Supplementary Information for

Bioinspired sulfur-surrounded iron catalyst for ammonia synthesis

*Na Zhang[a], Yubing Si[b], Qiang Fu[c], Xing Chen[a,]**

a. Institute of Molecular Plus, School of Chemical Engineering and Technology, Haihe Laboratory of Sustainable Chemical Transformations, Tianjin University, Tianjin 300192, PR China
b. College of Chemistry, Zhengzhou University, Zhengzhou 450001, PR China
c. School of Future Technology, University of Science and Technology of China, Hefei 230026, PR China

*: Corresponding Author, xing_chen@tju.edu.cn
Keywords: first principles, nitrogenase, NH_3 synthesis, bionic design

Outline of Supplementary Information

Section 1. Microkinetic Modeling Description

The reaction rate constant k is given by the Arrhenius equation

$$k = \frac{k_B T}{h} e^{\frac{-\Delta G_{TS}}{k_B}},$$

k_B is the Boltzmann constant, T is the temperature, h is the Plank constant, and ΔG_{TS} is the free energy of the transition state of the elementary step. The equilibrium constant for elementary step i is expressed by $K_i = \frac{k_i}{k_{-i}}$. The reaction rate of the elementary step can be expressed by

$$r_j = k_j \prod_i \theta_i^{v_i^j},$$

θ_i is the coverage of surface specie i, k_j is the rate constant, and v_i^j is the stoichiometry of species i in the elementary step j. The sum of coverage of reaction species and empty adsorption sites is equal to 1

$$\sum_i \theta_i + \theta^* = 1,$$

θ^* is the coverage of the empty site. In this study, we considered co-adsorption of intermediates, thus the reaction rate of elementary step i (*a/*b → *c/*d) can be expressed by $r_i = k_i \theta_{*a/*b} - k_{-i} \theta_{*c/*d}$.

Section 2. Electronic Structures of FeMo-co and Fe_3S_3 Cluster

2.1 Bader charge of FeMo-co and Fe_3S_3 cluster

The Bader charge distributions on the FeMo co-factor and Fe_3S_3 cluster are found in Table S1 and Table S2, respectively. Based on our findings, it is evident that the electrons transfer from Fe atoms to the surrounding S and center C atoms in FeMo-co. Similarly, in the case of the Fe_3S_3 cluster, the Bader charge analysis result reveals that electrons transfer from three Fe atoms to the S-rich environment. This observation is aligning with the electron transfer behavior observed between Fe and S atoms in the FeMo co-factor.

Table S1. The Bader charge of FeMo cofactor.

Atom	C	S_1	S_2	S_3	S_4	S_5	S_6	S_7	S_8	S_9
Bader Charge |e|	-0.83	-0.52	-0.50	-0.47	-0.47	-0.52	-0.52	-0.50	-0.53	-0.55
Atom	Fe_1	Fe_2	Fe_3	Fe_4	Fe_5	Fe_6	Fe_7	Mo_1	Fe_1	/
Bader Charge |e|	0.67	0.64	0.64	0.65	0.66	0.60	0.65	0.92	0.67	/

Table S2. Bader charge of the Fe_3S_3 cluster.

Atom	Bader Charge |e|
Fe_1	0.50
Fe_2	0.48
Fe_3	0.54
S_{18}	-0.67
S_{24}	-0.59
S_{26}	-0.64

2.2 PDOS of Fe atoms in the Fe_3S_3 cluster

The electronic partial density of states (PDOS) plots of Fe moiety indicate that the three Fe atoms are in the similar electronic states, as shown in Figure S1. Notably, all three Fe atoms with unpaired α (spin-up) electrons are spin-polarized. The spin polarization serves as a significant characteristic of the Fe atoms in the system.

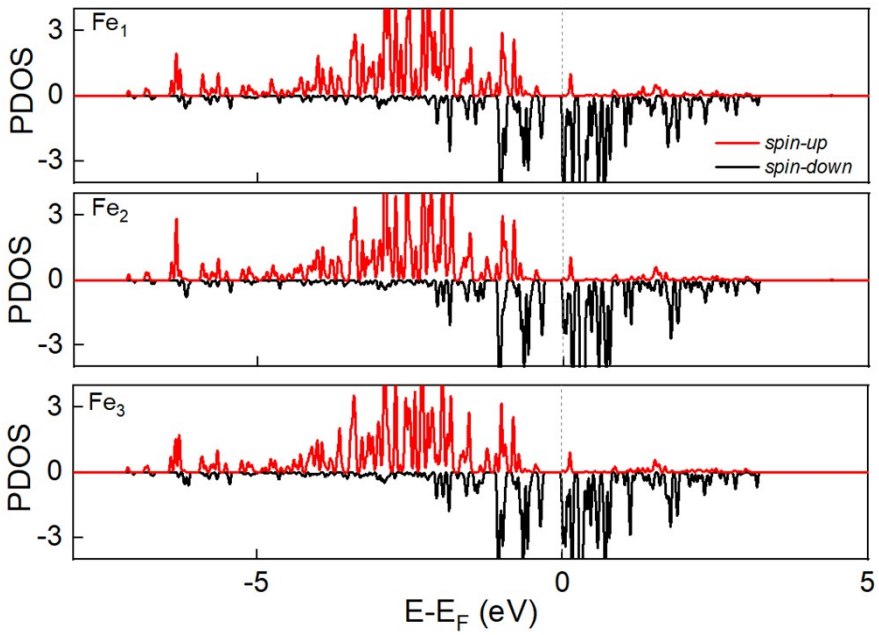

Figure S1. PDOS of the three Fe atoms of the Fe_3S_3 cluster. The red and black lines represent spin up and spin down, respectively.

Section 3. Stability of the Fe_3S_3 Cluster

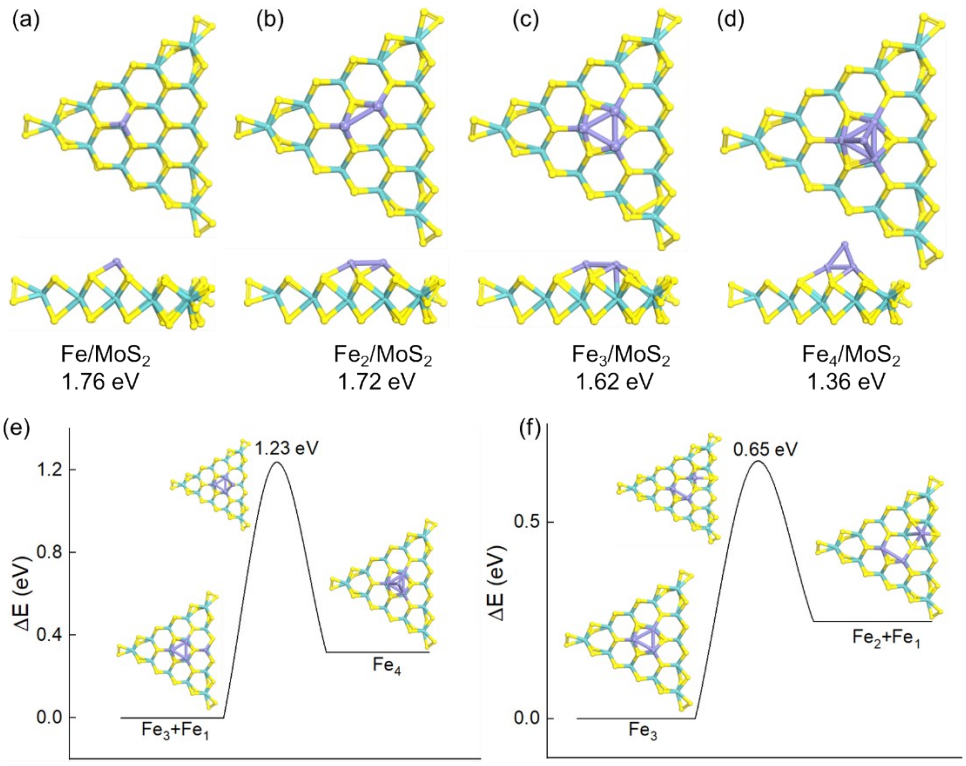

Figure S2. The Fe_3S_3 cluster is labeled as Fe_3/MoS_2 for comparison with other small clusters. Structures and the formation energy of possible clusters (a-d). Energy profile and corresponding

structures of (e) the aggregation of Fe_3 with Fe_1 to Fe_4, (f) the dissociation of Fe_3 into Fe_2 and Fe_1.

As displayed in Figure S2a-d, we investigated the formation energies of Fe/MoS_2, Fe_2/MoS_2, Fe_3/MoS_2, and Fe_4/MoS_2, respectively. We found that the formation energy per iron atom of Fe_3/MoS_2 is comparably among the cluster configurations mentioned above. We further discuss whether Fe_3/MoS_2 can be stabilized by kinetic effects. As shown in Figure S2e and S2f, the aggregation of Fe_3 with Fe_1 to Fe_4 clusters faces a challenging 1.23 eV kinetic barrier. Regarding the dissociation of Fe_3 to Fe_2 and Fe, its kinetic barrier is 0.65 eV. However, the energy of Fe_3/MoS_2 is 0.25 eV lower than that of Fe_2+Fe_1/MoS_2, indicating that the aggregation from Fe_2/MoS_2 to Fe_3/MoS_2 is favored over the dissociation. In summary, the Fe_3/MoS_2 cluster is stable and can be feasibly prepared on MoS_2 support.

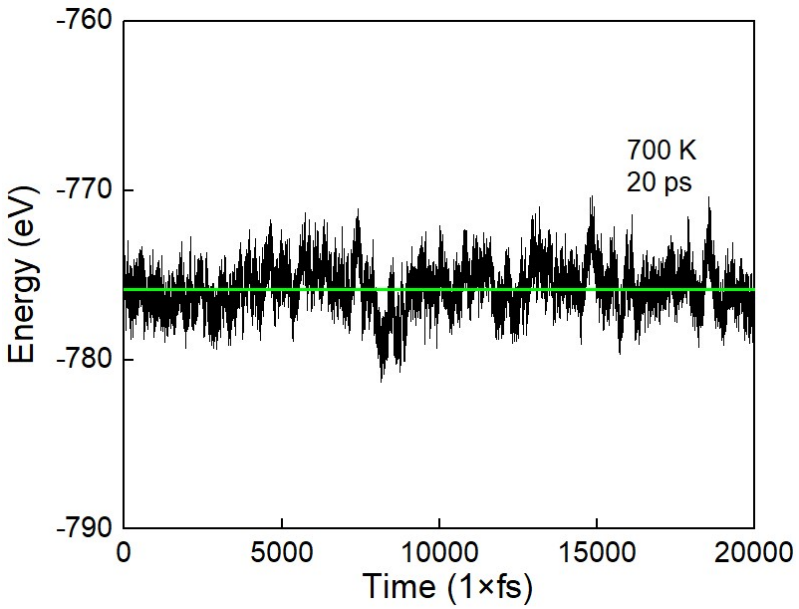

Figure S3. Energy evolution with AIMD simulation time under 700 K.

To confirm the stability of the Fe_3S_3 cluster under real reaction conditions, AIMD simulations were employed to evaluate its thermal stability for 20 *ps* within the NVT ensemble at a high temperature of 700 K (Figure S3). The structure of the Fe_3S_3 cluster remained largely unchanged throughout the simulation period. Notably, the Fe-related active site of the cluster was well preserved, further confirming its stability under the high-temperature conditions employed in the simulation. This observation suggests the Fe_3S_3 cluster exhibits robustness and maintains its catalytic properties over the course of the simulation.

Section 4. N_2 and H_2 Activation on the Fe_3S_3 Cluster

4.1 Possible N_2 adsorption configurations

In order to determine the most stable adsorption structure for N_2 activation, various adsorption states are considered. Among them, the side-on adsorption configuration (Figure S4d) is the most stable one with the lowest adsorption energy.

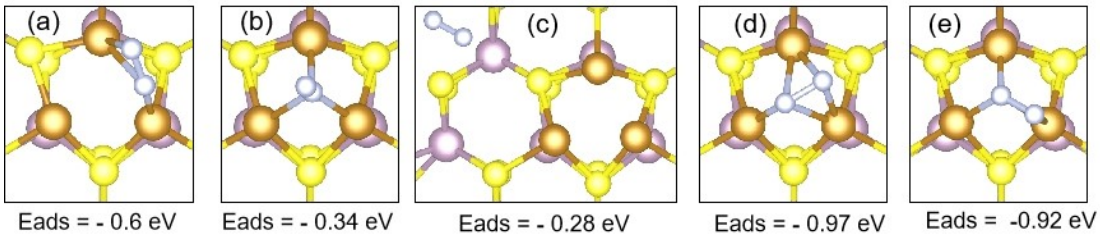

Figure S4. Considered N_2 adsorption states and their adsorption energies.

4.2 Bader charge of N_2 adsorption system

The Bader charge distributions on $*N_2/Fe_3S_3$ are presented in Table S3. When N_2 is chemisorbed on the Fe_3S_3 cluster, the electrons transfer from Fe atoms to the anti-bonding orbitals of N_2. The electron transfer weakens the stable N≡N bond. Specifically, the Bader charge of chemisorbed N_2 decreases to -0.87 |e|, as evidence of electron transfer from Fe to N_2.

Table S3. The Bader charge of $*N_2/Fe_3S_3$ complex.

Atom	Bader Charge |e|
Fe_1	0.31
Fe_2	0.28
Fe_3	0.26
S_{18}	-0.03
S_{24}	-0.11
S_{26}	-0.03
N_1	-0.3
N_2	-0.57

4.3 Electronic DOS of N_2 in free and adsorbed states

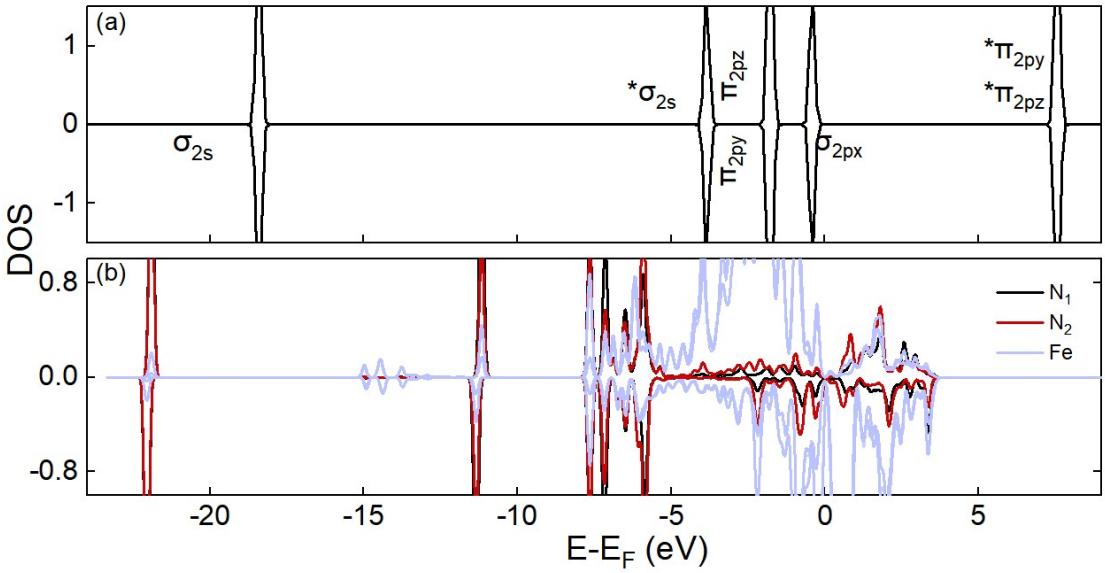

Figure S5. Electronic DOS of (a) free N_2 and (b) N_2/Fe_3S_3.

The activation of N_2 on the Fe_3S_3 cluster can be effectively explained through the analysis of the electronic density of states (DOS). As shown in Figure S5b, when N_2 is chemisorbed on Fe_3S_3, the degenerate π orbitals exhibit a significant degree of overlap with the *d* orbitals of Fe atoms. In the vicinity of the Fermi level, the π* orbitals strongly overlap with the *d* orbitals, indicating that electrons from the Fe atoms contribute to the anti-bonding state of N_2, thereby weakening the stable N≡N bond. In contrast to σ donation observed in the end-on adsorption configuration, π donation plays a predominant role in N_2 activation within the side-on adsorption configuration. The activated N_2 molecule exhibits spin-polarization due to the presence of unpaired β electrons near the Fermi level. The electronic configuration highlights the key role of π orbitals and demonstrates the spin-polarized nature of the activated N_2 molecule on the Fe_3S_3 cluster.

4.4 H_2 dissociation

We investigated the adsorption of H_2 on different sites, e.g., different S and Fe sites. As shown in Figure S6a, we considered all five inequivalent S adsorption sites, along with the Fe adsorption site for comparison. The adsorption structures and energies are displayed in Figure S6b-g. It is found that H_2 adsorbs more strongly on the S_3 site than on other S sites. However, the adsorption energy of H_2 on the Fe site is

-0.52 eV, which is 0.25 eV stronger than that on the S_3 site (-0.27 eV). This result indicates that H_2 adsorption prefers to occur on the Fe site of the Fe_3S_3 cluster.

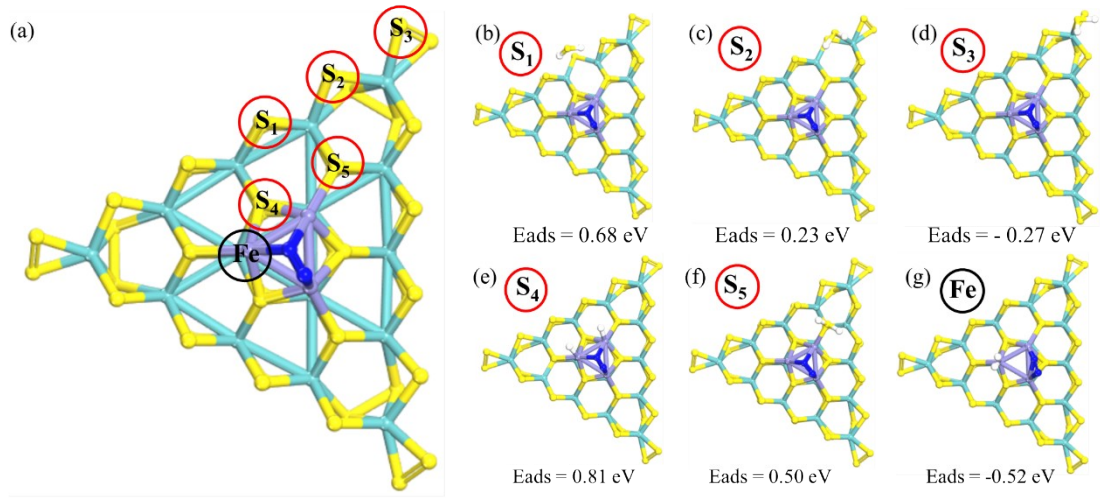

Figure S6. (a) Possible S adsorption sites on Fe_3@MoS_2. (b-g) The adsorption structures and energies of H_2 on various S and Fe sites.

H_2 dissociation is H_2 plays a critical role in the intermediate's hydrogenation process. In the Fe_3S_3 cluster, H_2 can be dissociated by a single Fe atom, accompanied by a change in the N_2 adsorption state (Figure S7a). As shown in Figure S7b, energy-resolved COHP is applied to evaluate H-H bond strength. In the free state of H_2, two electrons from two H atoms reside in the σ bonding state, while the σ* orbital remains unoccupied. However, upon adsorption, the σ* orbital becomes occupied as a result of the donated electrons from Fe *d* orbitals. The electron transfer leads to cleavage of the H-H bond. The calculated iCOHP value for this process is 0.26 eV, indicating the weakening of the H-H bond upon adsorption.

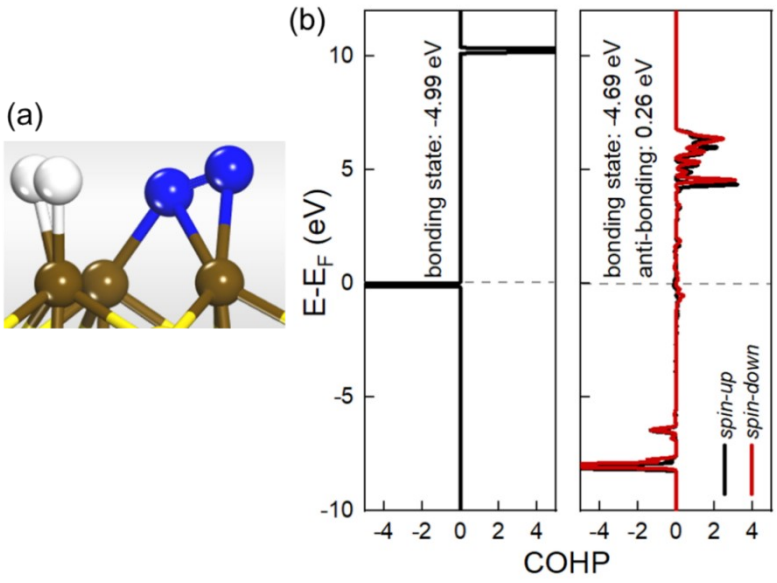

Figure S7. (a) Atomic structure of *N_2/2*H. (b) COHP of H-H bond in its free and adsorbed state. The positive and negative values represent the iCOHP of the bonding and anti-bonding state, respectively.

Section 5. Reaction Mechanism

5.1 All possible intermediates of associative pathway

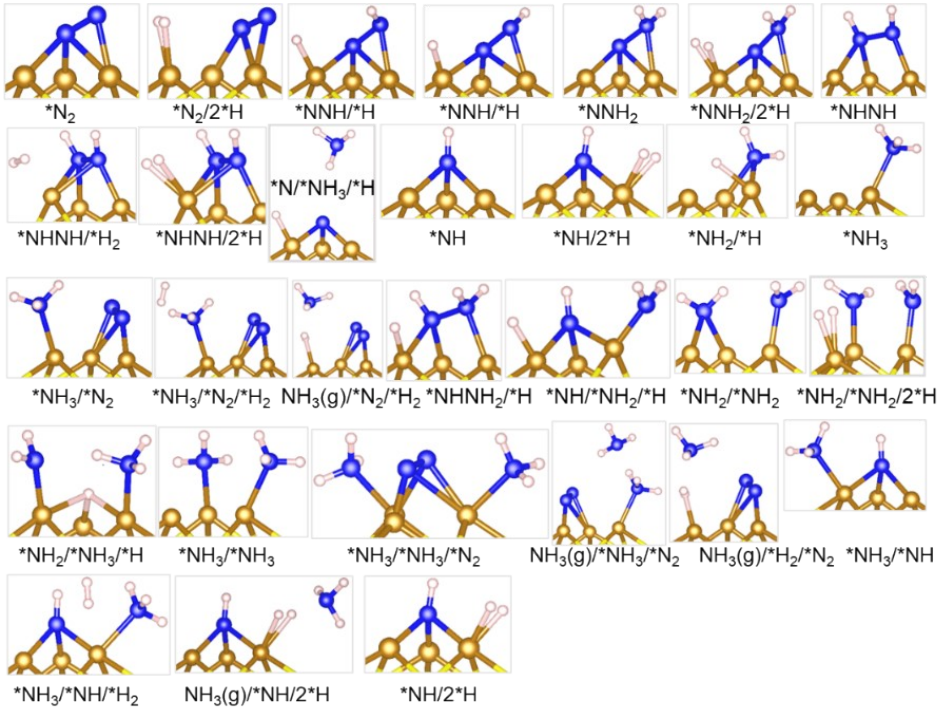

Figure S8. Stable adsorption structures of all intermediates.

In order to construct a comprehensive reaction network and identify the optimal reaction pathway for NH_3 synthesis, all possible intermediates were optimized. The calculated stable adsorption structures are depicted in Figure S8. By considering a wide range of potential intermediates, our reaction network analysis provides a thorough exploration of the NH_3 synthesis process.

5.2 Reaction energy diagram of four inferior reaction pathways

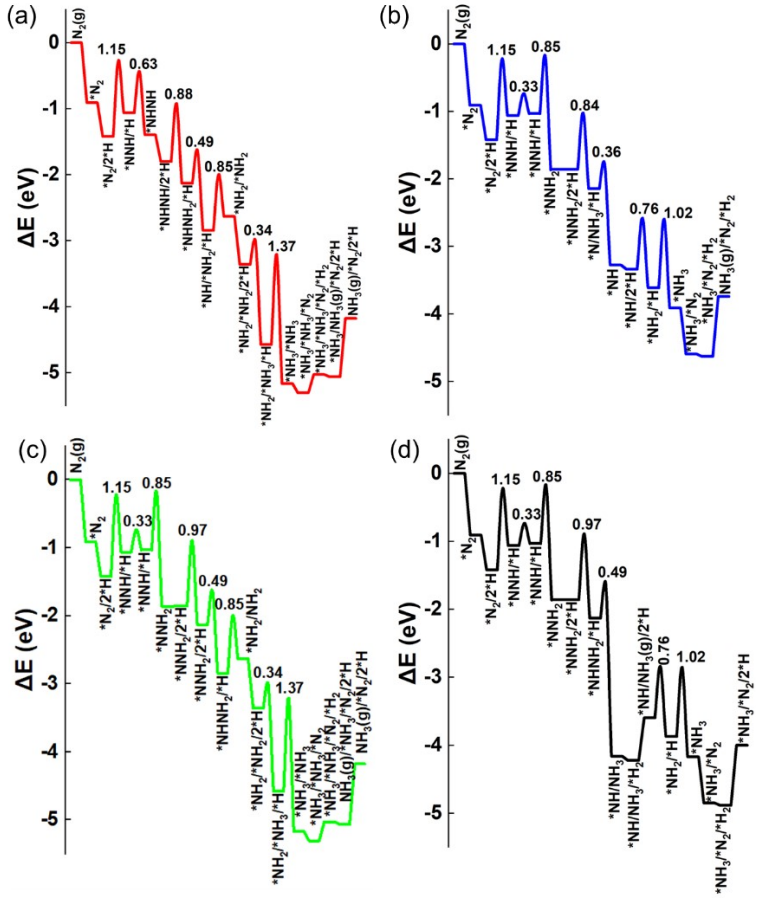

Figure S9. Energy diagram of NH_3 synthesis through (a) N_2 alternative hydrogenation via $*NH_2/*NH_2$ intermediates, (b) N_2 distal hydrogenation via $*N/NH_3(g)/*H$, (c) N_2 distal hydrogenation via $*NH_2/*NH_2$, and (d) N_2 distal hydrogenation via $*NH/*NH_3$.

In addition to the direct dissociation of N_2, we have constructed five associative reaction pathways based on the reaction network. Among them, four representative reaction paths are illustrated in Figure S9. From a thermodynamic perspective, the reaction pathways involving $*NNH_2$ or $*NH_2/*NH_2$ intermediates are considered less favorable. This can be attributed to the following reasons: (i) distal hydrogenation of *NNH to $*NNH_2$ is more challenging compared to the alternative hydrogenation pathway of *NHNH; (ii) hydrogenation of $*NHNH_2$ to $*NH_2/*NH_2$ requires

overcoming a high kinetic barrier (0.85 eV) compared to the hydrogenation of $*NHNH_2$ to $*NH/*NH_3$ (0.49 eV).

Overall, these thermodynamic considerations suggest that the reaction paths involving $*NNH_2$ or $*NH_2/*NH_2$ intermediates are less favorable compared to other pathways for NH_3 synthesis on the Fe_3S_3 cluster. Thus, the optimal reaction pathway contains *NNH alternative hydrogenation via *NHNH and $*NH/*NH_3$ intermediates.

5.3 Reaction energy and kinetic barrier of all elementary reactions

Table S4. Calculated reaction energies and kinetic barriers for all considered elementary steps.

Elementary step	ΔE (eV)	E_a (eV)
$N_2(g) \rightarrow *N_2$	-0.91	/
$*N_2/H_2(g) \rightarrow *N_2/2*H$	-0.51	/
$*N_2/2*H \rightarrow *NNH/*H$	0.36	1.15
$*NNH/*H \rightarrow *NNH/*H$	0.03	0.33
$*NNH/*H \rightarrow *NNH_2$	-0.83	0.85
$*NNH_2/H_2(g) \rightarrow *NNH_2/2*H$	0.0013	/
$*NNH_2/2*H \rightarrow *NNH_3/*H(*N/*H/NH_3(g))$	-0.28	0.84
$*N/*H \rightarrow *NH$	-1.13	0.36
$*NH/H_2(g) \rightarrow *NH/2*H$	-0.06	/
$*NH/2*H \rightarrow *NH_2/*H$	-0.27	0.76
$*NH_2/*H \rightarrow *NH_3$	-0.30	1.02
$*NH_3/N_2(g) \rightarrow *NH_3/*N_2$	-0.68	/
$*NH_3/*N_2/H_2(g) \rightarrow *NH_3/*H_2/*N_2$	-0.04	/
$*NH_3/*N_2/*H_2 \rightarrow NH_3(g)/ *N_2/2*H$	0.88	/
$*NNH/*H \rightarrow *NHNH$	-0.33	0.63
$*NHNH/H_2(g) \rightarrow *NHNH/2*H$	-0.40	/
$*NHNH/2*H \rightarrow *NHNH_2/*H$	-0.33	0.88
$*NHNH_2/*H \rightarrow *NH/*NH_2/*H$	-0.72	0.49
$*NH/*NH_2/*H \rightarrow *NH_2/*NH_2$	0.21	0.85
$*NH_2/*NH_2/H_2(g) \rightarrow *NH_2/*NH_2/2*H$	-0.73	/
$*NH_2/*NH_2/2*H \rightarrow *NH_2/*NH_3/*H$	-1.22	0.34
$*NH_2/*NH_3/*H \rightarrow *NH_3/*NH_3$	-0.59	1.37
$*NH_3/*NH_3/N_2(g) \rightarrow *NH_3/*NH_3/*N_2$	-0.14	/
$*NH_3/*NH_3/*N_2 \rightarrow *NH_3/NH_3(g)/*N_2$	0.28	/
$*NHNH_2/*H \rightarrow *NH/*NH_3$	-2.03	0.49

$*NH/*NH_3/H_2(g) \rightarrow *NH/*NH_3/*H_2$	-0.06	/
$*NH/*NH_3/*H_2 \rightarrow *NH/NH_3(g)/2*H$	0.63	/
$*NNH_2/2*H \rightarrow *NHNH_2/*H$	-0.27	0.97
$*N_2 \rightarrow 2*N$	2.51	/
$2*N + H_2(g) \rightarrow 2*N/2*H$	-0.49	/
$2*N/2*H \rightarrow *NH/*N/*H$	0.09	/
$*NH/*N/*H \rightarrow *NH/*NH$	-1.78	/
$*NH/*NH + H_2(g) \rightarrow *NH/*NH/2*H$	0.17	/
$*NH/*NH/2*H \rightarrow *NH_2/*NH/*H$	-1.49	/
$*NH_2/*NH/*H \rightarrow *NH_2/*NH_2$	-0.73	/
$*NH/*N/*H \rightarrow *NH_2/*N$	-2.64	/
$*NH_2/*N + H_2(g) \rightarrow *NH_2/*N/*H_2$	0.47	/
$*NH_2/*N/*H_2 \rightarrow *NH_3/*N/*H$	-0.62	/
$*NH_3/*N/*H \rightarrow *NH_3/*NH$	-2.56	/
$NH_2/*N/*H_2 \rightarrow NH_2/*NH/*H$	-0.93	/
$NH_2/*NH/*H \rightarrow NH_2/*NH_2$	-0.73	/

Section 6. Bader Charge Analysis

6.1 Functionality of Mo atoms for NH_3 production

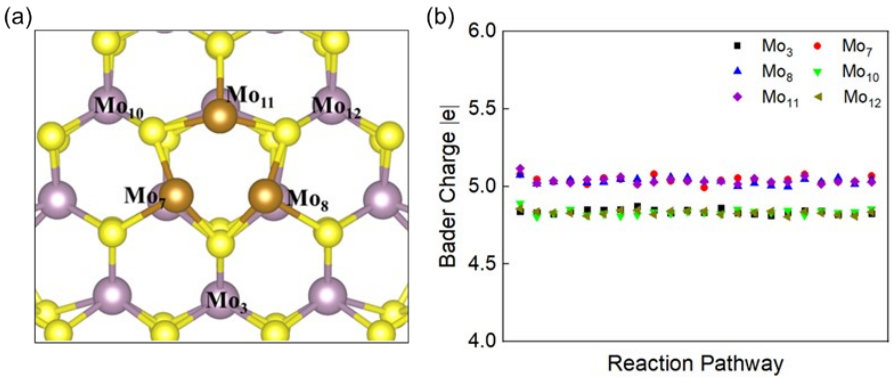

Figure S10. Bader charge variation of Mo atoms along with the optimal reaction pathway, the Mo atoms we selected are near the adsorption site.

To explore the function of the Mo atom in the reaction pathway, we selected the optimal reaction pathway and presented the Bader charge of Mo atoms near the adsorption site. We found that Bader charge slightly changes along the reaction pathway; thus, the Mo atoms in Fe_3S_3 cluster are likely to offer a scaffold instead of

the instead of tuning electronic structure.

6.2 Bader charge analysis for N_2 distal hydrogenation with *NH/*NH_3

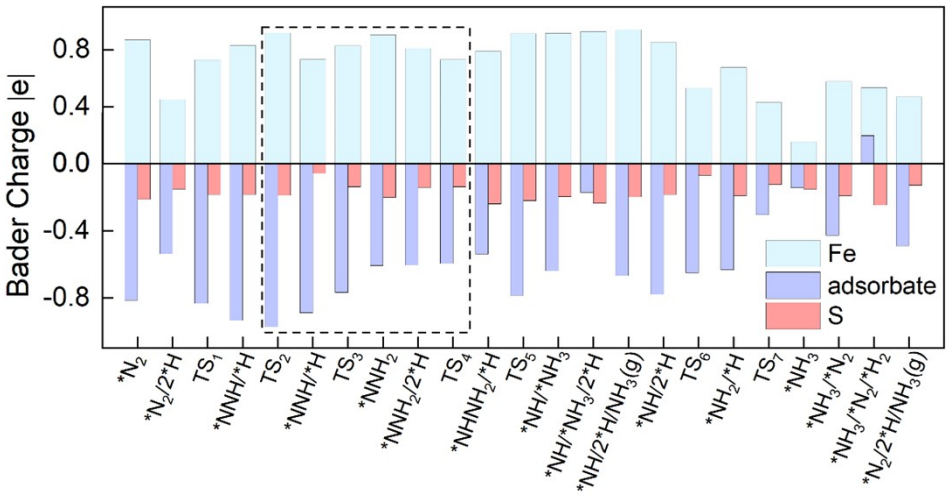

Figure S11. The Bader charge analysis of Fe, S, and adsorbate during the reaction pathway of N_2 distal hydrogenation with *NH/*NH_3.

Table S5. Bader charge of Fe, S, and adsorbates along the reaction pathway (alternative and distal).

N_2 alternative hydrogenation with NH/NH_3				N_2 distal hydrogenation with NH/NH_3			
	Fe	S	adsorbate		Fe	S	adsorbate
N_2	0.86898	-0.81448	-0.21305	N_2	0.86898	-0.81448	-0.21305
N_2/2H	0.45166	-0.53627	-0.15215	N_2/2H	0.45166	-0.53627	-0.15215
TS_1	0.73003	-0.83096	-0.18526	TS_1	0.73003	-0.83096	-0.18526
NNH/H	0.83142	-0.93328	-0.18451	NNH/H	0.83142	-0.93328	-0.18451
TS_2/0.63	0.78746	-0.74624	-0.20804	TS_2/0.33	0.917551	-0.972272	-0.188522
NHNH	0.95736	-0.7464	-0.23164	NNH/H	0.73331	-0.888717	-0.05899
NHNH/2H	0.79935	-0.57884	-0.23877	TS_3/0.85	0.828178	-0.766177	-0.138237
TS_3/0.88	0.79132	-0.58625	-0.19708	NNH_2	0.90395	-0.606794	-0.201122
$NHNH_2$/H	0.79001	-0.53762	-0.23957	NNH_2/2H	0.81002	-0.60445	-0.143404
TS_5	0.91296	-0.78356	-0.21975	TS_4/0.97	0.732707	-0.594738	-0.13794
NH/NH_3	0.91633	-0.63822	-0.1973	$NHNH_2$/H	0.79001	-0.53762	-0.23957
NH/NH_3/2*H	0.92724	-0.17086	-0.23657	TS_5	0.91296	-0.78356	-0.21975
*NH/2*H/NH_3(g)	0.94093	-0.66706	-0.199	*NH/*NH_3	0.91633	-0.63822	-0.1973
*NH/2*H	0.85148	-0.77863	-0.18489	*NH/*NH_3/2*H	0.92724	-0.17086	-0.23657
TS_6	0.53256	-0.64989	-0.06962	*NH/2*H/NH_3(g)	0.94093	-0.66706	-0.199
*NH_2/*H	0.67607	-0.63297	-0.19115	*NH/2*H	0.85148	-0.77863	-0.18489
TS_7	0.43135	-0.30354	-0.12432	TS_6	0.53256	-0.64989	-0.06962
*NH_3	0.15365	-0.14491	-0.15126	*NH_2/*H	0.67607	-0.63297	-0.19115
NH_3/N_2	0.57866	-0.42817	-0.19113	TS_7	0.43135	-0.30354	-0.12432
NH_3/N_2/*H_2	0.53486	0.16644	-0.24763	*NH_3	0.15365	-0.14491	-0.15126
N_2/H_2/NH_3(g)	0.47056	-0.48884	-0.12973	*NH_3/*N_2	0.57866	-0.42817	-0.19113
				NH_3/N_2/*H_2	0.53486	0.16644	-0.24763
				N_2/H_2/NH_3(g)	0.47056	-0.48884	-0.12973

N_2 alternative and distal hydrogenation with intermediate *NH/*NH_3 reaction pathways share some elementary steps. The elementary steps highlighted by the dashed rectangle only exist in the N_2 distal hydrogenation reaction pathway. The elementary step leading to $NHNH_2$ in the distal reaction mechanism undergoes a

higher energy barrier (0.97 eV) compared to the alternative reaction mechanism (0.88 eV in Figure 4c). The charge distribution on adsorbates significantly changes from -0.1434 |e| to -0.2396 |e| in the elementary step of the distal reaction. In contrast, the charge distribution roughly maintains in the alternative reaction. The substantial charge transfer could potentially hinder the reaction from NNH_2 to $NHNH_2$.

Section 7. Microkinetic Simulations

7.1 Coverage of surface species of the optimal reaction pathway

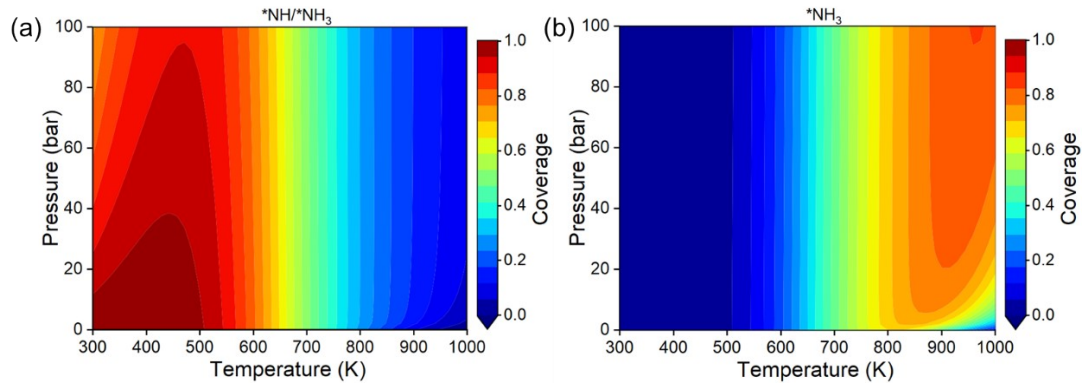

Figure S12. Coverage of surface species correlated with temperature and pressure. Coverage of (a) $*NH/*NH_3$ and (b) $*NH_3$ on Fe_3S_3 cluster mapped at the pressure of 1-100 bar and the temperature of 300-1000 K. the N_2's partial pressure is fixed at 25% and NH_3 conversion is set to 2%.

Excessively stable adsorption of surface species on the catalyst surface can impose limitations on catalytic performance. At high temperature of 900 K, the TOF of the Fe_3S_3 cluster is predominantly constrained by $*NH_3$ intermediates. However, at low temperatures within the range of 300-500 K, the TOF is less than 10^{-10} $s^{-1}site^{-1}$. The small TOF value is primarily attributed to the stable adsorption of $*NH/*NH_3$ intermediate on the catalyst surface. The strong adsorption hinders the desired catalytic reactions and impedes the overall catalytic performance of the Fe_3S_3 cluster at the low temperature range.

7.2 Microkinetic modeling of other four reaction pathways

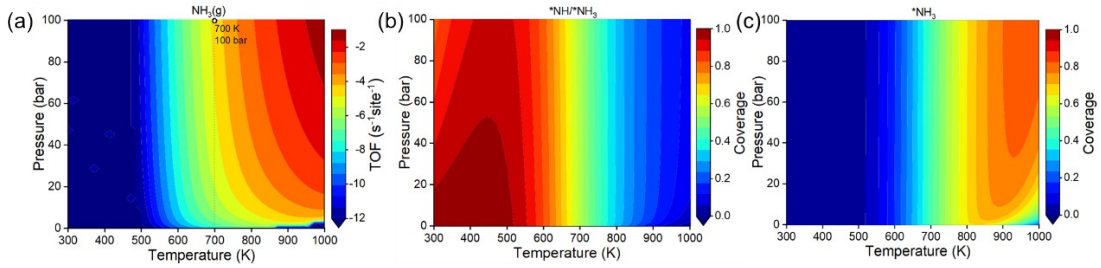

Figure S13. TOF of the Fe_3S_3 cluster for NH_3 production and coverage of surface species correlated with temperature and pressure. (a)TOF for NH_3 production through N_2 distal hydrogenation via *NH/*NH_3 mapped at the temperature of 300-1000 K and the pressure of 0-100 bar. Coverage of (b) *NH/*NH_3 and (c) *NH_3 in reaction pathway on Fe_3S_3 cluster.

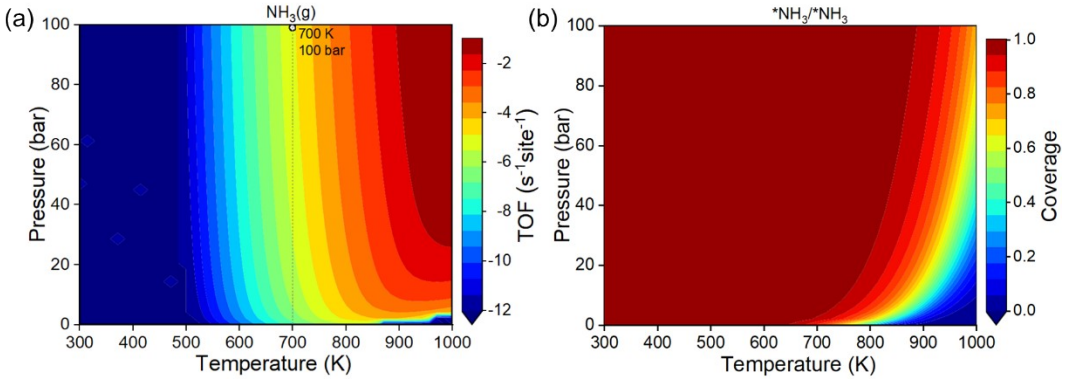

Figure S14. TOF of the Fe_3S_3 cluster for NH_3 production and coverage of surface species correlated with temperature and pressure. (a) TOF for NH_3 production through N_2 alternative hydrogenation via NH_2/NH_2 mapped at the temperature of 300-1000 K and the pressure of 0-100 bar. (b) Coverage of *NH_3/*NH_3 in reaction pathway on Fe_3S_3 cluster.

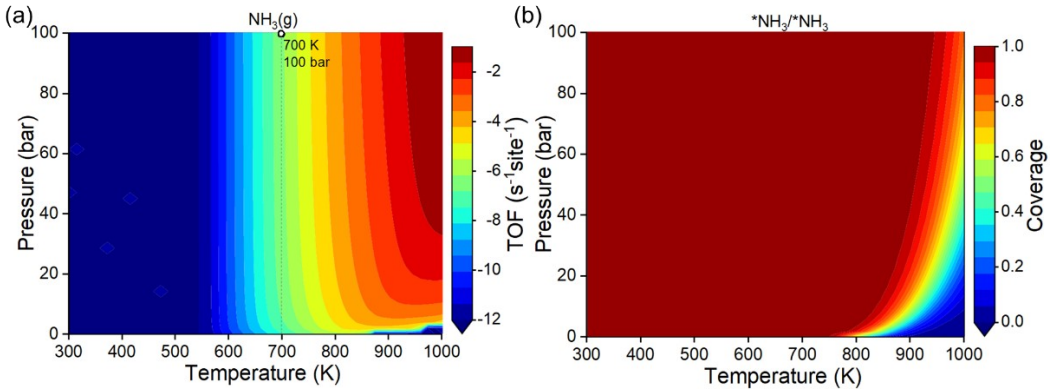

Figure S15. TOF of the Fe_3S_3 cluster for NH_3 production and coverage of surface species correlated with temperature and pressure. (a) TOF for NH_3 production through N_2 distal hydrogenation via NH_2/NH_2 mapped at the temperature of 300-1000 K and the pressure of 0-100 bar. (b) Coverage of *NH_3/*NH_3 in reaction pathway on Fe_3S_3 cluster.

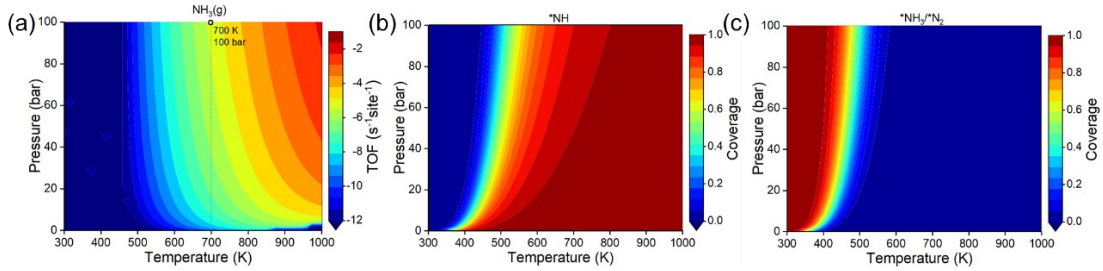

Figure S16. TOF of the Fe_3S_3 cluster for NH_3 production and coverage of surface species correlated with temperature and pressure. (a) TOF for NH_3 production through N_2 distal hydrogenation via N/H/NH_3(g) mapped at the temperature of 300-1000 K and the pressure of 0-100 bar. Coverage of (b) *NH and (c) *NH_3/*N_2 in reaction pathway on Fe_3S_3 cluster.

7.3 Comparison of catalyst performance for NH_3 production

Table S6. Comparison of catalyst performance for NH_3 production in previous studies and this work.

Catalyst	TOF ($site^{-1}\cdot s^{-1}$)	Feed gas composition	Conversion ratio of NH_3	Temperature (K)	Ref.
Fe_3/Al_2O_3	1.4×10^{-2}	1:3 (N_2:H_2)	10%	700	42
Fe (211)	2.65×10^{-3}	1:3 (N_2:H_2)	10%	700	42
Ti/ (8, 8) BNNT	2.98×10^{-6}	1:3 (N_2:H_2)	10%	700	76
Mo_2/Ag	1.1×10^{-3}	1:3 (N_2:H_2)	2%	673	81
Fe_3S_3	4.4×10^{-4}	1:3 (N_2:H_2)	2%	700	This work